Acta Pharmaceutica Sinica B 2025;15(11):5988−6000

Chinese Pharmaceutical Association
Institute of Materia Medica, Chinese Academy of Medical Sciences

Acta Pharmaceutica Sinica B

www.elsevier.com/locate/apsb
www.sciencedirect.com

ORIGINAL ARTICLE

Electrochemical biosensors with right-side-out-oriented cell membrane coating for the evaluation of AChE inhibitors as potential anti-Alzheimer's disease agents

Ying Zhao[a], Xia Liu[a], Shuning Yang[a,b], Jiabo Wang[a,b], Dan Wu[a,b], Yusi Bu[a,b,*], Xiaoyu Xie[a,b,c,*]

[a]*School of Pharmacy, Health Science Center, Xi'an Jiaotong University, Xi'an 710061, China*
[b]*Shaanxi Engineering Research Center of Cardiovascular Drugs Screening & Analysis, Xi'an 710061, China*
[c]*Key Laboratory of Environment and Genes Related to Diseases (Xi'an Jiaotong University), Ministry of Education, Xi'an 710061, China*

Received 15 January 2025; received in revised form 30 May 2025; accepted 20 June 2025

KEY WORDS

Red blood cell membranes;
Right-side-out-oriented cell membrane coating;
Electrochemical biosensors;
Immunological affinity;
Alzheimer's disease;
Traditional Chinese medicines;
Acetylcholinesterase inhibitors;
Drug evaluation

Abstract Biosensors based on acetylcholinesterase (AChE) are crucial for early diagnosis, less invasive treatment, and drug evaluation of Alzheimer's disease (AD). However, existing technologies often suffer from enzyme conformational changes, leading to altered activity and loss and reduced sensor efficacy. To address this challenge, we developed a novel right-side-out-oriented red blood cell membrane-coated electrochemical biosensors (ROCMCBs) to evaluate AChE inhibitors from traditional Chinese medicines (TCMs) as potential anti-AD agents. The developed right-side-out-oriented coating based on immunoaffinity not only fully exposed the binding sites of AChE on the cell membrane but also ensured its conformation and stability as a peripheral membrane-anchoring protein, which was conducive to maintaining its biological activity and producing optimal interaction with drugs. At the same time, the biosensors exhibited a satisfactory sensitivity (limit of detection = 0.41 pmol/L). Ultimately, six potentially active compounds against AD (baicalin, geniposide, gastrodin, berberine, rhynchophylline, and senkyunolide A) were rapidly identified and evaluated from TCMs. This project provides a promising strategy for developing cell membrane-coated electrochemical biosensors. The application of cell membrane-coated electrochemical biosensors with well-defined cell membrane orientation further expands new perspectives and methods for AChE-targeted anti-AD research.

*Corresponding authors.
E-mail addresses: buyusi@xjtu.edu.cn (Yusi Bu), xiexiaoyu@xjtu.edu.cn (Xiaoyu Xie).

Peer review under the responsibility of Chinese Pharmaceutical Association and Institute of Materia Medica, Chinese Academy of Medical Sciences.

https://doi.org/10.1016/j.apsb.2025.09.032

1. Introduction

Alzheimer's disease (AD) is a prevalent neurodegenerative disorder characterized by systemic dementia manifestations, such as memory impairment, executive dysfunction, and changes in personality and behavior[1,2]. The loss of cholinergic neurons reduces acetylcholine (ACh) levels, correlating strongly with cognitive decline in AD patients[3,4]. It is known that acetylcholinesterase (AChE, E.C. 3.1.1.7) is a serine protease with aminopeptidase and carboxypeptidase activities. Its primary function is to hydrolyze ACh as a neurotransmitter to terminate nerve conduction[5]. Numerous approved drugs for the treatment of AD are associated with the inhibition effect of AChE. For instance, huperzine A can inhibit AChE and effectively alleviate AD[6]. Since AChE plays a critical role in the cognitive decline observed in AD patients, targeted evaluation and precise measurement of its activity can lay the groundwork for the development of more specialized anti-AD drugs. A variety of analytical techniques have been developed for AChE assay, including UV-Vis spectrophotometry[7], fluorescence method[8], and colorimetric method[9]. However, under physiological conditions, the primary functional form of AChE is an amphiphilic tetramer anchored to the cell membranes[10,11]. Once dissociated from the cell membranes, AChE undergoes conformational changes that alter its function. This limits the ability of current methods to quantitatively assess AChE expression under conditions that reflect actual biological activity. Consequently, there is a critical need to develop a straightforward and practical anti-AD drug evaluation method based on the actual biological activity of AChE.

Currently, cell membrane camouflage technology is increasingly being employed as a top-down approach, leveraging natural cell membranes to enhance the biointerface capabilities of nanoparticles[12,13]. This method faithfully preserves the complexity of the membrane, endowing membrane-coated nanoparticles with many of the source cell's inherent characteristics[14]. This method typically involves coating nanoparticles with cell membranes derived from sources such as red blood cells (RBCs)[15], platelets[16], or cancer cells[17]. RBCs are the most abundant type of blood cell. They lack the nucleus and most organelles, and their plasma membrane is highly biocompatible[18]. Recently, electrochemical platforms based on natural cell membranes have been developed, offering advantages in terms of simplicity, rapidity, and sensitivity. These platforms have the potential to minimize nonspecific biomolecule adsorption and offer a biocompatible interface for enzyme expression detection[19]. Accordingly, they can provide a more biomimetic method for detecting the actual biological activity of AChE. Additionally, they exhibit considerable promise and offer distinct benefits when it comes to screening or evaluating potentially active compounds from natural products[20-22]. However, the random orientation of the cell membrane coating method hinders effective drug binding due to the asymmetric nature of cell membranes. Existing cell membrane-based electrochemical platforms often overlook this orientation issue during electrode coating[23]. Consequently, the reconstruction of oriented cell membranes on biosensor surfaces represents a significant challenge that requires continued investigation.

In recent years, the directed assembly of cell membrane-coated nanoparticles has been achieved through various methods, including freeze-thaw cycles[24], ultrasonication[25], extrusion, and electroporation[26]. These techniques have been extensively studied and applied, driving advancements in the field of biomimetic nanoparticles for diverse biomedical applications. However, these methods subject the electrode material to mechanical and thermal stresses, which may result in damage to the material or structural changes on the surface of the electrode. Such changes will affect the surface morphology, the degree of exposure of the active sites, the catalytic performance, and the cycling stability of the electrode. Furthermore, covalent binding immobilization of cell membranes has been employed in the fabrication of electrochemical biosensors[27-29]. This method of immobilization is robust, yet it may compromise the conformation or activity of the proteins. Hence, considering the damage to the electrode and the retention of peripheral membrane-anchored protein AChE activity, achieving oriented assembly of cell membranes on the electrode surface is another key issue.

In this study, we designed right-side-out-oriented red blood cell membranes-coated electrochemical biosensors (ROCMCBs) to accurately measure the biological activity of AChE. This platform is particularly focused on the evaluation of inhibitors, playing a crucial role in anti-AD research. The specific orientation not only maximized the exposure of the peripheral membrane anchoring protein AChE, enhancing its conformation and catalytic activity, but also protected the structure of the electrode. Scheme 1 illustrated the operational schematic of the assay. Briefly, the right-side-out-oriented assembly of red blood cell membrane (RBCM) on the surface of glassy carbon electrodes (GCEs) was achieved through immunoaffinity interaction. Compared to random-oriented red blood cell membrane-coated electrochemical biosensors (CMCBs), ROCMCBs demonstrated enhanced redox activity due to the increased exposure of AChE's active sites. Furthermore, ROCMCBs also exhibited a sensitive detection limit for huperzine A as low as 0.41 pmol/L. We also discussed the practical advantages of this method for cell membrane-coated electrochemical biosensors. This study highlights the evaluation of AChE inhibitors, potentially expands the application of cell membrane biomimetic technology in electrochemical biosensors, and provides novel insights into evaluating potentially active compounds from traditional Chinese medicines (TCMs) and investigating their mechanisms of action.

2. Materials and methods

2.1. Collection of RBCM

The collection of RBCM was carried out as previously described[30]. Specifically, fresh blood was first collected and transferred into a centrifuge tube containing anticoagulants. The whole blood was then centrifuged at 1000×*g* for 10 min at 4 °C to separate the RBCs from the plasma. The resulting precipitates were collected and washed 3 times with 1 × phosphate-buffered saline (PBS, pH 7.4) at 4 °C to isolate pure RBCs. These washed

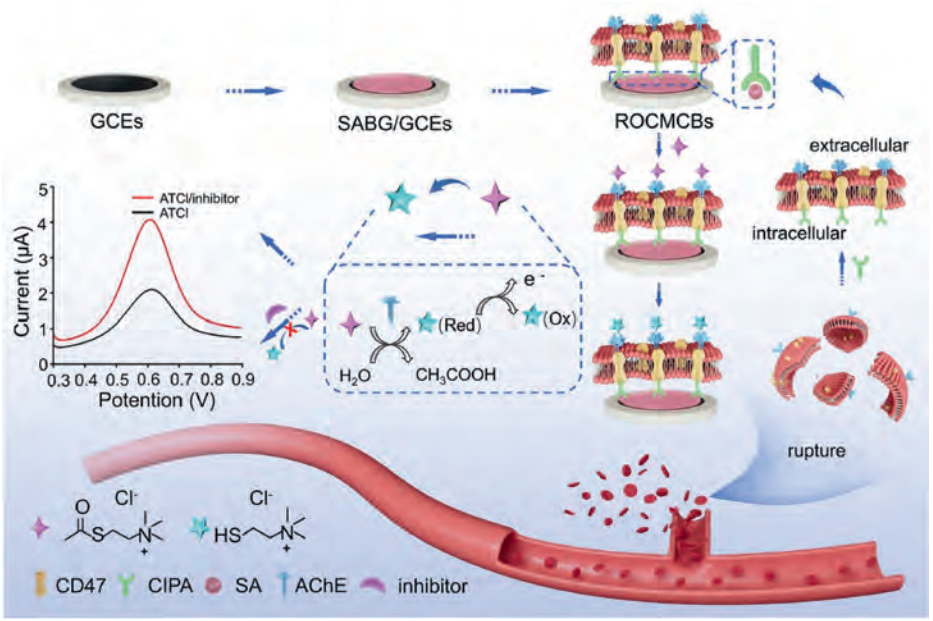

Scheme 1 Schematic representation of the preparation and application of ROCMCBs for potential anti-Alzheimer's disease (AD) drug evaluation.

RBCs were fully suspended in 0.25 × PBS and stored at 4 °C. Due to osmotic pressure on the plasma membrane, the RBCs swelled and underwent hemolysis. The suspension was subsequently centrifuged at 12,000×*g* for 20 min at 4 °C, and the supernatant was discarded. Finally, the RBCM was washed with 1 × PBS, and this process was repeated 3 times. The isolated RBCM was stored at 4 °C for temporary use.

2.2. *Fabrication of ROCMCBs*

Prior to modification, the GCEs were polished to a mirror finish using alumina slurries with particle sizes of 1.0, 0.3, and 0.05 μm. Following each polishing step, the GCEs were subjected to ultrasonic cleaning in dilute nitric acid, ethanol, and double-distilled water sequentially for 3 min each. The electrodes were then dried under a nitrogen atmosphere.

Subsequently, the secondary antibody (gold-conjugated secondary antibody against rabbit IgG, SA) was diluted with 0.5% bovine serum albumin (BSA), after which glutaraldehyde was added to form the SA-BSA-glutaraldehyde (SABG) solution. After thorough mixing, 8 μL SABG was dripped on the GCEs and left to air dry at room temperature. Glutaraldehyde was used to facilitate the firm adhesion of SA to the surface of the GCEs. In parallel, the cluster of differentiation 47 (CD47) intracellular primary antibody (CIPA) was mixed with RBCM and incubated at 37 °C for 1 h to achieve full binding to the CD47 receptors on the RBCM surface. 8 μL CIPA/RBCM were then dripped on the SABG/GCEs. The electrodes were left at room temperature for 2 h, followed by 3 rinses with PBS. Due to the immunoaffinity between the antibodies, ROCMCBs were successfully prepared by coating RBCM on the surface of SABG/GCEs in a right-side-out orientation.

2.3. *The immunofluorescence validation of ROCMCBs*

In this experiment, CD47 was selected as a marker of membrane orientation. CD47 is a transmembrane receptor with a heavily glycosylated N-terminal IgV-like extracellular domain and a diminutive C-terminal intracellular domain[31,32], which is widely expressed in human cells, including RBCs. Initially, RBCM were labeled with the membrane dye 1,1′-dioctadecyl-3,3,3′,3′-tetramethylindocarbocyanine perchlorate (DiI) to mark them in red. Next, complete ROCMCBs and CMCBs were assembled separately, with at least 2 of each type. The CIPA and CD47 extracellular primary antibody (CEPA) solutions were then applied to the surface of each group of sensors, followed by incubating at room temperature for 2 h and washing 3 times with PBS. Subsequently, the Alexa Fluor 405-labeled SA (AFSA) was introduced and incubated in the dark for 30 min to prevent fluorescence quenching. This was followed by another set of 3 PBS washes to remove any residues. Finally, the fluorescence on the sensor surfaces was examined with a confocal laser scanning microscope (CLSM), and the fluorescence intensity was quantified with ImageJ. This procedure was repeated 3 times to ensure the reproducibility.

2.4. *Biosensor assay procedure*

Electrochemical impedance spectroscopy (EIS), cyclic voltammograms (CV), and differential pulse voltammetry (DPV) measurements were carried out using a CHI-660E electrochemical workstation, which was purchased from Shanghai CH Instruments Ins. (Shanghai, China). GCEs with 3 mm diameter were used as the working electrode. A platinum wire served as the counter electrode, and an Ag/AgCl electrode (1 mol/L KCl) was employed as the reference electrode.

EIS measurements were conducted in 0.1 mol/L PBS (pH 7.4) containing 5.0 mmol/L $[Fe(CN)_6]^{3-/4-}$ and 0.1 mol/L KCl. The applied AC impedance varied from 10 to 1,000,000 Hz with an amplitude of 50 mV at a constant potential of 0 V. CV was carried out in the same solution, scanning from −0.2 to 0.6 V. For all experiments, a 3.0 mL electrolyte solution was used. The optimum concentration of 5.0 mmol/L acetylthiocholine (ATCl) was prepared in 0.1 mol/L PBS (pH 7.4). Due to the redox reaction

between the substrate and AChE, a distinct oxidation peak at 650 mV was detected using the DPV method. The reaction equation based on ATCl is shown in Eq. (1). Initially, ATCl is hydrolyzed by AChE to thiocholine (TCh) and acetic acid (HA). Subsequently, according to Eq. (2), TCh is further oxidized to its dimer (dithiobischoline) on the electrode surface.

$$ATCl + H_2O \xrightarrow{AChE} TCh + HA + Cl^- \quad (1)$$

$$2TCh(red) \rightarrow TCh(ox) + 2H^+ + 2e^- \quad (2)$$

2.5. Electrochemical response of huperzine A on ROCMCBs

Huperzine A, a reversible cholinesterase inhibitor with selective inhibitory effects on AChE, was selected as a positive drug[6]. 2.0 mg huperzine A was accurately weighed and dissolved in 2.0 mL of 0.1 mol/L PBS (pH 7.4) in a centrifuge tube to prepare a 4.1 mmol/L stock solution. The stock solution was added to 0.1 mol/L PBS (pH 7.4) containing 5.0 mmol/L ATCl and diluted to obtain solutions with concentrations of 8.2 μmol/L, 4.1 μmol/L, 820.0 nmol/L, 410.0 nmol/L, 82.0 nmol/L, 41.0 nmol/L, 4.1 nmol/L, 410.0 pmol/L, and 41.0 pmol/L, respectively. The inhibition of the current response of ROCMCBs at 650 mV by different concentrations of huperzine A was tested with DPV, and the inhibition rates were calculated using Eq. (3):

$$\text{Inhibition}\ (\%) = \frac{I_{max} - I_{min}}{I_{max}} \times 100 \quad (3)$$

where I_{max} is the current measured under optimal substrate conditions (5.0 mmol/L ATCl), I_{min} is the steady-state current following the addition of huperzine A.

The Michaelis-Menten constant (K_m) for ROCMCBs was obtained by analyzing the standard current-time curve at 650 mV after incrementally adding ATCl to 0.1 mol/L PBS (pH 7.4) while stirring. Then, the K_m value was determined using the Lineweaver-Burk equation [Eq. (4)]:

$$\frac{1}{I_S} = \frac{K_m}{I_{max}} \frac{1}{C} + \frac{1}{I_{max}} \quad (4)$$

where I_s is the steady-state current following substrate addition, I_{max} is the peak current measured at saturated substrate conditions, and C is the bulk concentration of the substrate.

2.6. Optimization of experimental conditions

To optimize RBCM concentration, a series of RBCM suspensions with concentrations of 0.5, 1.0, 1.5, 2.0, 2.5, and 3.0 mg/mL were prepared. The absorbance of each suspension was determined using a spectrophotometer to ensure uniformity and appropriate transmittance. The peak currents were compared at different concentrations using DPV.

Then, a concentration-peak current curve was constructed to determine the optimal cell membrane concentration. Subsequently, the effect of huperzine A inhibition time on ROCMCBs was optimized. Here, the current difference (ΔI) was defined in Eq. (5):

$$\Delta I = I_0 - I_1 \quad (5)$$

where I_0 is the peak current of ATCl prior to the incubation of ROCMCBs with huperzine A, and I_1 is the peak current of ATCl at the same sensor after incubation with huperzine A.

Additionally, the buffer solution PBS was precisely adjusted to pH values of 5.5, 6.0, 6.5, 7.0, 7.4, and 8.0. The peak currents of ROCMCBs at different pH values were compared, and pH-peak current curves were constructed to determine the optimal solution pH value. Simultaneously, the peak currents of ROCMCBs were assessed at different temperatures, including 4, 25, 37, and 50 °C. A temperature-peak current curve was constructed to determine the optimal incubation temperature. Each experiment was conducted 3 times for reliability.

2.7. Selectivity, reproducibility, and stability of ROCMCBs

Huperzine A, galanthamine, nitrofurazone, oxytetracycline, and indomethacin were accurately weighed. Each compound was dissolved in 0.1 mol/L PBS (pH 7.4) in centrifuge tubes to prepare initial solutions with a concentration of 4.1 mmol/L. These stock solutions were then diluted with 0.1 mol/L PBS (pH 7.4) containing 5.0 mmol/L ATCl to obtain final solutions with a concentration of 4.1 μmol/L. Ultimately, 4.1 μmol/L huperzine A, galanthamine, nitrofurazone, oxytetracycline, and indomethacin were employed to assess the selectivity of ROCMCBs and CMCBs, respectively. The peak currents of their response to ATCl under the same conditions were compared to assess the reproducibility of the sensors. The experiment was repeated 3 times. Then, to evaluate the storage stability of ROCMCBs, the inhibitory responses of 4.1 μmol/L huperzine A on ROCMCBs and CMCBs were measured daily over the course of seven consecutive days, with inhibition rates calculated accordingly. The entire experiment was repeated 3 times.

2.8. Molecular docking study

Molecular docking was conducted using SYBYL-X 2.0 (Tripos, MO, USA) to investigate the interaction between potentially active compounds from different kinds of TCMs and AChE. The AChE structure used for docking was retrieved from the Protein Data Bank (PDB). In the process of preparing the protein, eutectic ligands and water molecules were removed, while hydrogen atoms were added. The side chains underwent adjustments, and the AMBER7 FF99 force field was employed. Drug molecule structures were drawn and integrated into the Tripos force field, and Gasteiger-Hückel charge types were assigned to facilitate energy minimization. Surflex-Dock was employed for molecular docking studies. Finally, the binding interactions between drug ligands and AChE protein were visualized using PyMOL (Schrödinger LLC, OR, USA).

2.9. Inhibitors' evaluation of ROCMCBs

Baicalin, geniposide, gastrodin, berberine, senkyunolide A, rhynchophylline, tanshinone IIA, and echinacoside were accurately weighed and dissolved in 0.1 mol/L PBS in centrifuge tubes to prepare initial solutions, respectively. These stock solutions were then diluted with 0.1 mol/L PBS (pH 7.4) containing 5.0 mmol/L ATCl to achieve target concentrations of 2.2, 4.5, 9.0, 22.4, 44.8, and 89.6 μmol/L for baicalin; 2.6, 3.9, 5.2, 6.5, 12.9, and 25.7 μmol/L for geniposide; 0.9, 1.8, 3.5, 5.2, 7.0, and 14.0 μmol/L for gastrodin; 1.0, 1.5, 3.0, 9.9, 14.9, and 29.7 μmol/L for berberine; 0.5, 5.2, 26.0, 52.0, 130.0, and 260.0 μmol/L for senkyunolide A; 2.6, 5.2, 26.0, 65.0, 130.0, and 260.0 μmol/L for rhynchophylline; 1.7, 17.0, 85.0, 170.0, 340.0, and 680.0 μmol/L for tanshinone IIA; 0.1, 1.3, 12.7, 127.0, 254.0, and 635.0 μmol/L for echinacoside. Due to the inhibition of enzyme activity, the DPV current response to different concentrations of selected

ingredients was diminished. The inhibition rates of selected ingredients were calculated using Eq. (3), respectively.

2.10. Statistical analysis

Data were analyzed using Origin 2024b (OriginLab Corp., MA, USA) and GraphPad Prism Software 9.5 (GraphPad Software Inc., CA, USA) and presented as mean ± standard error of the mean (SD). The study assessed significant differences between the two groups using Student's *t*-test and employed one-way analysis of variance (ANOVA) for multiple comparisons. The differences at $P < 0.05$ were considered statistically significant (ns, no statistical difference; $*P < 0.05$, $**P < 0.01$, and $***P < 0.001$).

3. Results and discussion

3.1. Corroboration of right-side-out-oriented RBCM coating of ROCMCBs

An oriented coating of cell membranes allows receptor proteins and sensing elements to be arranged orderly, improving the recognition of specific molecules and enhancing sensor sensitivity. In contrast, random coating may hinder the specificity of the prepared electrochemical sensor, making it harder to distinguish similar compounds from complexes. Additionally, oriented coating techniques can also form a stable membrane layer, boosting the mechanical stability and durability of the prepared electrochemical sensor. Therefore, CLSM, scanning electron microscope (SEM), EIS, and DPV experiments were used to investigate the orientation of RBCM coating. Here, the CD47 receptor was selected as a marker for delineating the RBCM orientation of ROCMCBs. Fig. 1A presented a schematic depiction of immunofluorescence assays of ROCMCBs and CMCBs designed to investigate the coating orientation of RBCM.

Fig. 1B showed the CLSM results of ROCMCBs. As we could see, blue fluorescence was observed in the ROCMCBs group after incubation with CEPA and AFSA. However, less blue fluorescence was observed after incubation with CIPA and AFSA. It could be inferred that only the extracellular portion of CD47 receptors remained on the surface of ROCMCBs after SABG was coated with RBCM with a right-side-out orientation. In contrast, blue fluorescence was observed in the CMCBs group after incubation with CEPA/CIPA and AFSA (Fig. 1C), revealing that both intracellular and extracellular portions of CD47 receptors were retained on the surface of CMCBs. The SEM analysis depicted in Fig. 1D revealed microscopic scratches on the surface of the

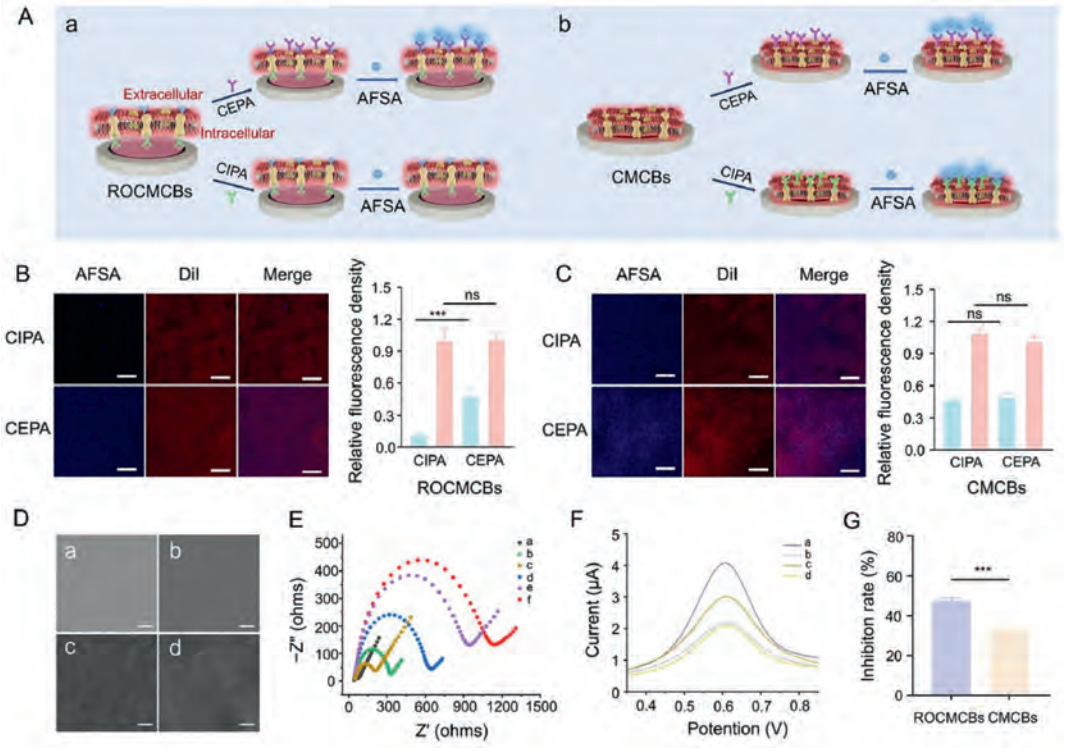

Figure 1 Corroboration of the right-side-out-oriented coating. (A) Schematic demonstration of the orientation of RBCMs coating by immunofluorescence assays. (B) CLSM images and quantification of fluorescence intensity of ROCMCBs. Scale bar = 5 μm. (C) CLSM images and quantification of fluorescence intensity of CMCBs. Scale bar = 5 μm. (D) SEM images of bare GCEs (a), SABG/GCEs (b), CMCBs (c), and ROCMCBs (d). Scale bar = 2 μm. (E) The Nyquist plots under different incubation methods including bare GCEs (a), RBCMs droplet was incubated with GCEs for 2 h, followed by washing with PBS and drying with nitrogen atmosphere (b), RBCMs droplet was overnight incubated with GCEs at 4 °C and humid conditions to avoid complete sample evaporation (c), RBCMs droplet was overnight incubated for complete sample drying at room temperature (d), RBCMs droplet was overnight incubated with SABG/GCEs for complete sample drying at room temperature (e), and RBCMs droplet was incubated with SABG/GCEs for 2 h, followed by washing with PBS and drying with nitrogen atmosphere (f). (F) DPV curves of ROCMCBs (a) and CMCBs (c) in 5.0 mmol/L ATCl. And DPV curves of ROCMCBs (b) and CMCBs (d) in 5.0 mmol/L ATCl with 4.2×10^{-8} mol/L huperzine A. (G) Quantification of current signal inhibition rates in (F). Data are presented as mean ± SD ($n = 3$). $***P < 0.001$; ns, not significant.

uncoated electrode (Fig. 1Da), whereas the surface of SABG/GCEs exhibited a complete and uniform SABG coating (Fig. 1Db). The surface of ROCMCBs (Fig. 1Dd) achieved a flatter and more consistent RBCM coverage compared to CMCBs (Fig. 1Dc). These observations underscored the stable deposition of RBCM on ROCMCBs.

Typically, RBCM adheres to gold electrodes either through electrostatic adsorption[33] or covalent interactions[34,35], such as gold-sulfur bonds. However, the surface of GCEs lacks the interactive capability to maintain the RBCM coating during the application. When the RBCM is simply drop-coated on the GCEs, perturbations in the electrical stimulation may lead to dislodgement and inefficiency challenges. Thus, EIS experiments evaluated different cell membrane coating techniques on GCEs. As we could see in Fig. 1E, the right-side-out-oriented coating method based on immunoaffinity achieved a high charge transfer resistance of up to 1200 ohms for ROCMCBs (curve f) compared to the other four different coating methods (curves b−e) and bare GCEs (curve a), verifying that the right-side-out-oriented coating method was the most efficient method. In addition, to further demonstrate the superiority of the right-side-out-oriented coating method, the electrochemical behaviors of ROCMCBs and CMCBs were investigated using the DPV method in 5.0 mmol/L ATCl. As depicted in Fig. 1F, ROCMCBs (curves a and b) exhibited a significantly higher current response compared to CMCBs (curves c and d) under identical experimental conditions. This enhancement could be primarily attributed to the right-side-out-oriented coating method, which prevented detachment and improved the stability of ROCMCBs. Moreover, Fig. 1G provided a quantitative visual representation of current inhibition rates. The above experiments demonstrated that the RBCM were coated on ROCMCBs with a right-side-out orientation, exhibiting excellent electrochemical performance. This right-side-out orientation method is of significant importance for the evaluation of AD inhibitors.

3.2. *Fabrication and characterization of ROCMCBs*

To investigate the immobilization of AChE on ROCMCBs, RBCM underwent staining procedures using a specific primary antibody (AChE monoclonal antibody, MA3-042) followed by an SA (Alexa Fluor 488-labeled goat anti-rabbit) compatible for immunofluorescence analysis. The samples were incubated with a DiI staining reagent to stain RBCM. CLSM results indicated that RBCM was labeled with red fluorescence (Fig. 2Aa), while AChE was labeled with green fluorescence (Fig. 2Ab). The distinct colocalization of red and green signals (Fig. 2Ac) confirmed that AChE resided on the RBCM, establishing the basis for using ROCMCBs in evaluating anti-AD drugs. Moreover, an energy-dispersive spectroscopy (EDS) analysis was conducted. The EDS maps of ROCMCBs are shown in Fig. 2B, and the EDS maps of SABG and RBCM are shown in Supporting Information Figs. S1 and S2. Obviously, SABG contained five elements, which were C, O, N, S, and P, while RBCM contained only four elements, which were C, O, N, and P. The homogeneous distribution of C, O, N, S, and P elements in ROCMCBs suggested the successful decoration of RBCM on SABG.

In order to research the surface structure and properties of ROCMCBs, the atomic force microscope (AFM) analysis was adapted, and the results were presented in Fig. 2C. It was observed that the average thickness of the SABG layer was approximately 2 nm (Fig. 2Ca). Upon the addition of the RBCM layer, the total thickness increased by approximately 10 nm (Fig. 2Cb), which indicated that RBCM were successfully integrated into ROCMCBs. Then, the coating process was detected by Fourier transform infrared spectroscopy (FT-IR) spectroscopy, as shown in Fig. 2D. The spectra of SABG, CIPA/RBCM, and ROCMCBs showed peaks in the range of 2800−3000 cm^{-1}, which corresponded to C−H vibrations in membrane proteins and lipids (Fig. 2Da), along with those in the range of 1080−1085 cm^{-1}, associated with phospholipid C−O−C vibrations (Fig. 2Db), were

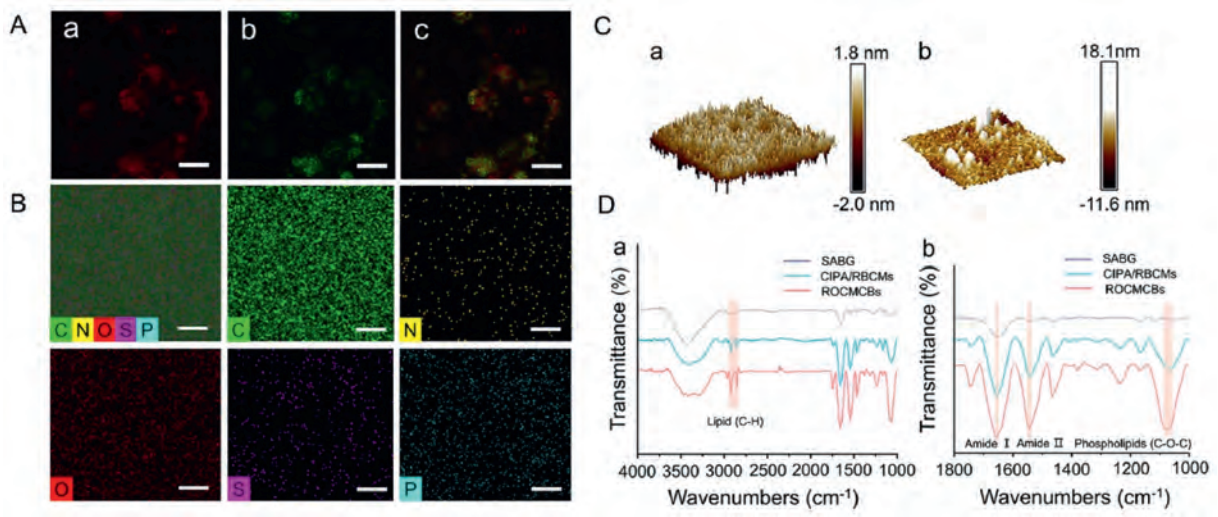

Figure 2 Fabrication and characterization of ROCMCBs. (A) CLSM images of ROCMCBs: red fluorescence labelled by DiI represented the existence of RBCMs (a), green fluorescence labelled by Alexa Fluor 488-labeled goat anti-rabbit represented the existence of AChE (b), and colocalized image (c). Scale bar = 5 μm. (B) EDS mapping of C, N, O, P, and S elements in ROCMCBs. Scale bar = 5 μm. (C) AFM images of SABG (a) and ROCMCBs (b). (D) FTIR investigation of wavelength 4000−1000 cm^{-1} (a) and 1800−1000 cm^{-1} (b).

completely preserved on CIPA/RBCM and ROCMCBs. Meanwhile, the peaks identified in the ranges of 1600−1700 cm^{-1} and 1510−1580 cm^{-1} (Fig. 2Db) represent amide I and amide II bands, respectively. The above results were consistent with the previous reports[36,37], indicating that the proteins of RBCM were not destroyed excessively during the hemolysis and washing process. Obviously, the characteristic spectral features within RBCM were effectively preserved, and ROCMCBs were built successfully.

3.3. *Antifouling properties of ROCMCBs*

Antifouling interfaces play a crucial role in the use of biosensors for drug evaluation. They significantly enhance the precision and reliability of ROCMCBs, thereby greatly improving their efficiency and accuracy for drug screening. The CLSM images revealed significant nonspecific protein adsorption on bare GCEs (Fig. 3Aa) and SABG/GCEs (Fig. 3Ab), with a distinct green fluorescence. In contrast, minimal fluorescence was observed on CMCBs (Fig. 3Ac) and ROCMCBs (Fig. 3Ad). Quantitative analysis in Fig. 3B quantificationally confirmed that ROCMCBs had significantly lower fluorescence intensity compared to bare GCEs and SABG/GCEs, similar to control groups (FITC-BSA labeled CMCBs). The results underscored the effective protein-repelling properties exhibited by the RBCM coating.

Fundamentally, constructing an antifouling surface of ROCMCBs involves creating a hydrophilic interface[38]. Water contact angles were measured across various material-modified sensors to demonstrate robust hydrophilicity on the surfaces of ROCMCBs. As indicated in Fig. 3Ca, the bare GCEs exhibited an initial angle of 64.6°. The angle decreased to 46.8° upon modification using SABG (Fig. 3Cb). Moreover, after being coated with RBCM, the water contact angles of ROCMCBs and CMCBs were down to 22.1° (Fig. 3Cc) and 28.6° (Fig. 3Cd), respectively. These findings underscored that ROCMCBs provided compelling groundwork for developing antifouling sensing interfaces. At the same time, wettability is also a critical parameter for improving the biocompatibility of materials[39], which plays a significant role in determining how effectively materials interact with biological components, such as cells and tissues. The small water contact angle could also reflect the ROCMCBs' good wettability. Therefore, the RBCM-modified interface could improve the biocompatibility of the electrode and enhance the performance of the prepared electrochemical biosensor.

3.4. *Optimization of experimental conditions*

A key factor in the preparation of the electrochemical biosensor is the quantity of AChE on ROCMCBs. To investigate this, the influence of RBCM concentration, from 0.5 to 3.0 mg/mL, was studied in 0.1 mol/L PBS (pH 7.4) with 5.0 mmol/L ATCl. As illustrated in Fig. 4A and B, the current response grew as the RBCM concentration increased and reached a maximum of approximately 2.0 mg/mL. However, it decreased significantly with the further increase of RBCM concentration. This could be due to the increased resistance of the electrochemical process due to the thicker RBCM layer. Therefore, 2.0 mg/mL was selected as the ideal concentration.

The effect of inhibition time on the prepared electrochemical biosensor response is also one of the most important parameters. Therefore, the effect of inhibition on AChE activity at different incubation times (5−30 min) was examined separately in 4.1 μmol/L huperzine A. The dependence of incubation time on current differences was illustrated in Fig. 4C and D. The results demonstrated that the inhibitory effect of huperzine A on AChE increased with incubation time, eventually plateauing after 25 min. This indicated that the enzyme binding to the active target site was saturated after 25 min. Thus, an incubation duration of 25 min was chosen as the optimal parameter.

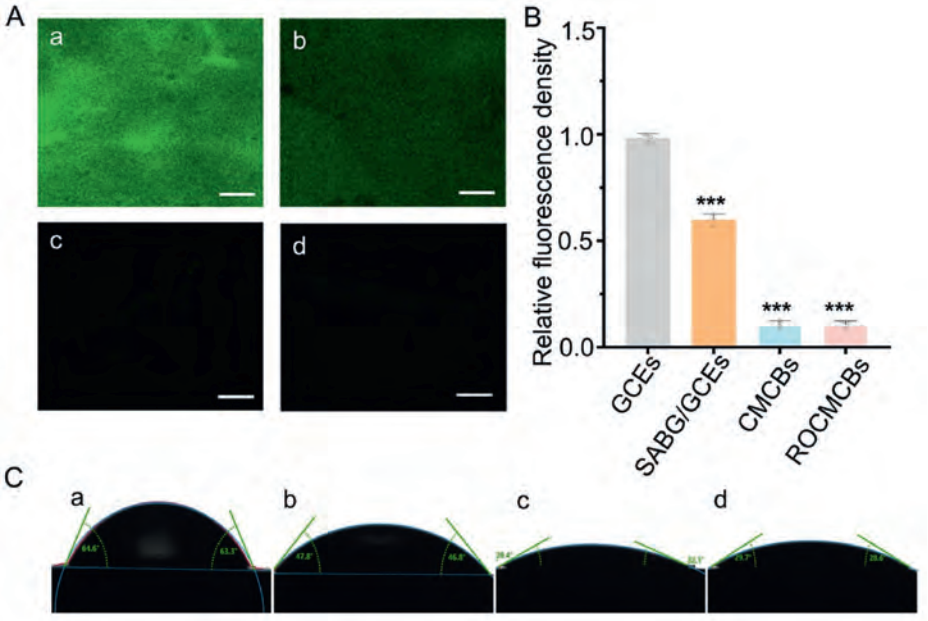

Figure 3 Antifouling properties of ROCMCBs. (A) CLSM images of bare GCEs (a), SABG/GCEs (b), CMCBs (c), and ROCMCBs (d) after soaking in FITC-labeled BSA solution. Scale bar = 50 μm. (B) Quantitative analysis of (A). (C) Contact angle images of bare GCEs (a), SABG/GCEs (b), CMCBs (c), and ROCMCBs (d). Data are presented as mean ± SD ($n = 3$). ***$P < 0.001$; ns, not significant.

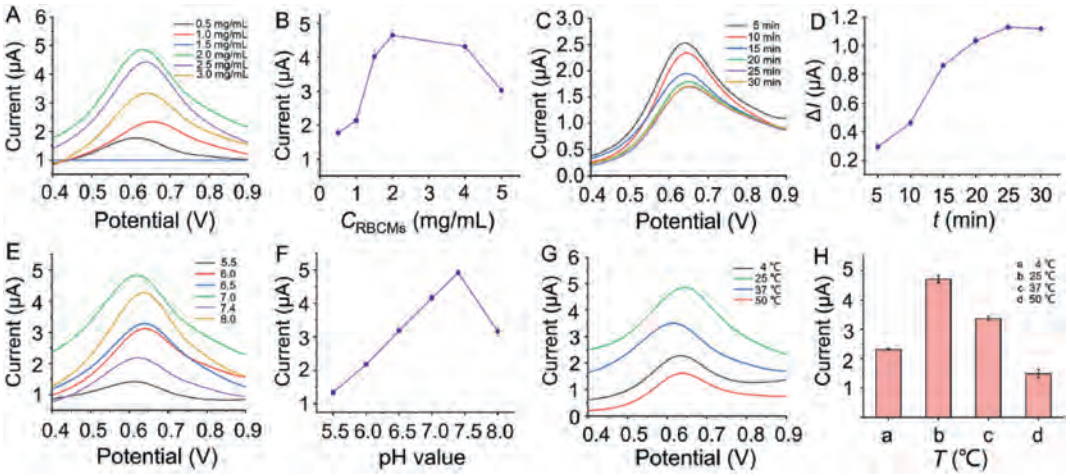

Figure 4 Optimization of experimental conditions of ROCMCBs. (A, B) RBCM concentration from 0.5 to 3.0 mg/mL. (C, D) The incubation time with huperzine A. (E, F) pH and (G, H) temperature on the amperometric response. Data are presented as mean ± SD (n = 3).

In addition, it is widely recognized that the biological activity of immobilized AChE is influenced by both the pH and temperature of the solution. Thus, the relationship between the catalytic peak current of AChE for the ATCl reaction and the pH value or temperature of the solution was investigated. Notably, within the pH range of 5.5 to 8.0, the maximum peak current occurred at pH 7.4 (Fig. 4E and F). In addition, 4, 25, 37, and 50 °C were tested, and the highest peak current was recorded at 25 °C. The results were shown in Fig. 4G and H. Consequently, the solution with pH 7.4 and temperature of 25 °C was selected for subsequent experiments.

3.5. *Electrochemical behavior of ROCMCBs*

The mechanism underlying the redox reaction between the enzyme AChE and its substrate ATCl involves ATCl being hydrolyzed by AChE into TCh and HA. Subsequently, TCh

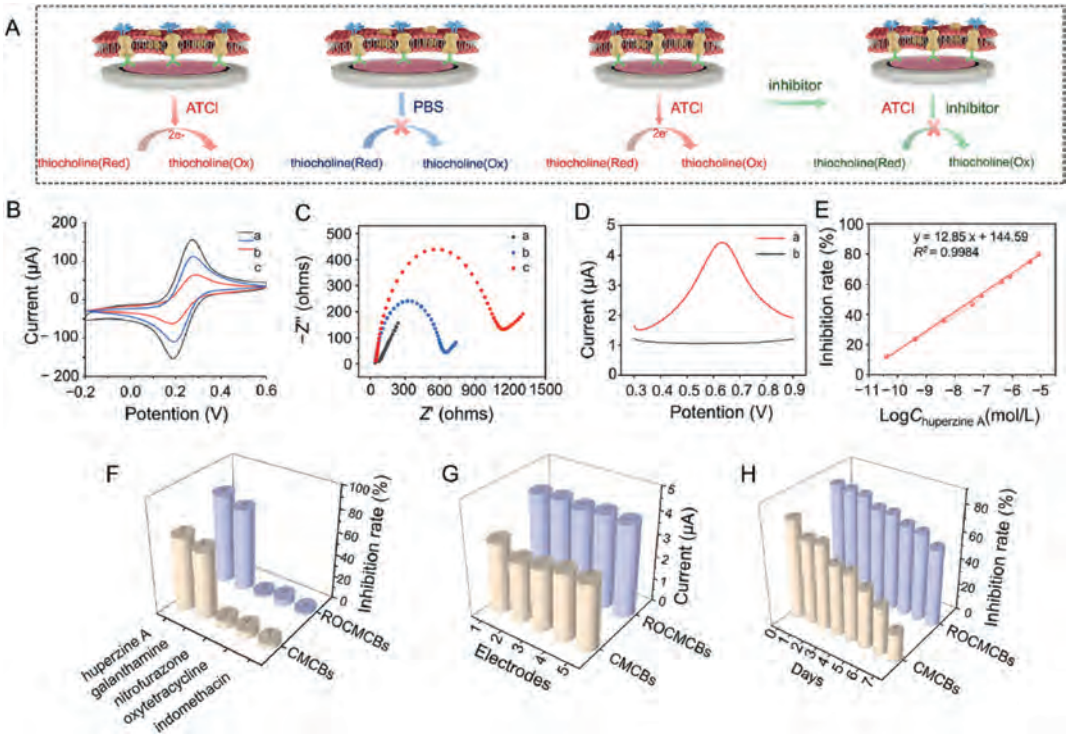

Figure 5 Electrochemical behavior of ROCMCBs. (A) Schematic diagram of the specific reaction of AChE with ATCl. (B) CVs and (C) the Nyquist plots of bare GCEs (a), SABG/GCEs (b), and ROCMCBs (c) in 3.0 mL of 5.0 mmol/L $[Fe(CN)_6]^{3-/4-}$. (D) DPV curves of ROCMCBs in 3.0 mL of 5.0 mmol/L ATCl (a) and 0.1 mol/L PBS (b). (E) The relationship between peak currents and concentrations of huperzine A. (F) Selectivity investigation of ROCMCBs and CMCBs. (G) Reproducibility investigation of ROCMCBs and CMCBs. (H) Stability investigation of ROCMCBs and CMCBs. Data are presented as mean ± SD (n = 3).

undergoes oxidation, forming TCh(ox)[40]. This particular redox reaction requires the presence of ATCl and not just in PBS. Furthermore, if AChE activity is suppressed by an inhibitor, this reaction similarly ceases. Fig. 5A schematically illustrates these concepts.

The step-by-step construction of ROCMCBs was analyzed using CV and EIS in a solution of 0.1 mol/L KCl and 5 mmol/L $[Fe(CN)_6]^{3-/4-}$. Fig. 5B showed the CV results, indicating a decrease in peak current and reversibility with the modification of SABG (curve b) and CIPA/RBCM (curve c) compared to bare GCEs (curve a). The EIS results in Fig. 5C displayed Nyquist plots for different sensors, where the charge transfer resistance (R_{ct}) was calculated from the semicircle diameter. Bare GCEs (Fig. 5Ca) exhibited a low R_{ct}, appearing nearly linear on EIS analysis. Conversely, when SABG was immobilized onto GCEs using glutaraldehyde, an increase in impedance coupled was observed due to the low conductivity of SABG (Fig. 5Cb). Further impedance increase was observed after coating with CIPA/RBCM (Fig. 5Cc). The CV and EIS results corresponded to each other, indicating that ROCMCBs were constructed successfully step by step.

Subsequently, the electrochemical behavior of ROCMCBs was assessed in the presence and absence of 5.0 mmol/L ATCl. DPV in Fig. 5D showed a strong oxidation peak of AChE at 650 mV (curve a), which was ascribed to the electrochemical oxidation of the electroactive TCh. Meanwhile, there was no significant current response of AChE in the electrolyte without substrate ATCl (curve b). Furthermore, as shown in Supporting Information Fig. S3, the CVs of various biosensors demonstrated the absence of redox peaks without ATCl. However, with the addition of 3 mL 5.0 mmol/L ATCl, ROCMCBs exhibited an irreversible oxidation peak at 650 mV, unlike bare GCEs and SABG/GCEs. Then, the impact of scan rates on ROCMCBs in 0.1 mol/L PBS with 5.0 mmol/L ATCl was investigated in Supporting Information Fig. S4. The results revealed that the oxidation of TCh occurred as an irreversible electrode reaction, evidenced by a single oxidation peak. Additionally, the oxidation peak current of TCh increased with scan rates varying from 10 to 100 mV/s, suggesting a diffusion-controlled process for ATCl oxidation on ROCMCBs. A linear relationship between the TCh peak oxidation current (I_{pa}) and the square root of the scan rate ($\nu^{1/2}$) was confirmed by the plot, supporting the diffusion-controlled nature of the oxidation process ($R^2 = 0.9934$, $n = 3$).

In addition, by continuously adding substrate (ATCl) to the stirred cell, the typical current-time response curves for ROCMCBs were obtained. As depicted in Supporting Information Fig. S5, the addition of ATCl to ROCMCBs prompted a rapid and sensitive current response, indicating the swift diffusion of reaction products (ACh)[41]. Notably, the amperometric response showed a linear increase within the concentration range of 1 to 5 mol/L as the concentration of ATCl increased ($R^2 = 0.9799$). The K_m, which reflects the enzymatic activity of AChE when reacting with ATCl as a substrate, was calculated as 1.995 mmol/L according to Eq. (4). The small value of K_m implied that AChE immobilized on ROCMCBs maintained its catalytic activity and exhibited a greater affinity for ATCl. Comparisons of K_m of ROCMCBs with other previously reported biosensors based on AChE were shown in Supporting Information Table S1. Notably, AChE used in previously reported sensors was isolated through purification processes and exhibited well-defined enzymatic activity as well as lower K_m values. In contrast, although the K_m value of RBCM-anchored AChE in this study was slightly higher, it could maintain the native spatial conformation of AChE to closely mimic physiological conditions and meet the experimental requirements for subsequent evaluation of AChE inhibitors.

3.6. Electrochemical response of huperzine A for ROCMCBs

The relationship between the rate of inhibition and the concentration of anti-AD drugs was evaluated using huperzine A as a model compound. As shown in Fig. 5E, with an increase in the concentration of huperzine A in the ATCl solution, the generation current of AChE decreased. Under the optimized experimental conditions, the inhibitory effect of huperzine A on AChE was proportional to its concentration (from 8.2 μmol/L to 41 pmol/L). The linear equation was given by: Inhibition rate (%) = 12.85 log$C$ + 144.59, $R^2 = 0.9984$. The limit of detection (LOD) was approximately 0.41 pmol/L ($S/N = 3$).

To the best of our knowledge, it turns out to be very difficult to fabricate pure AChE on RBCM to replace commercial AChE for anti-AD drug evaluation. In comparison with previously reported purified AChE sensing platforms in Supporting Information Table S2, our proposed strategy not only maintained the authentic biological activity of AChE as a peripheral membrane-anchored protein but also demonstrated comparable sensitivity (LOD = 0.41 pmol/L), which was essential for accurate assessment of AChE's function and interactions. The above results indicated that the designed ROCMCBs were competent in detecting low abundance AChE. By leveraging the advantages of easy acquisition and cost-effectiveness of RBCM, our method offers promising applications for ultrasensitive biomedical assays.

3.7. Selectivity, reproducibility, and stability of ROCMCBs

The ability to selectively recognize ROCMCBs is essential for real applications. Huperzine A and galantamine[41] are known inhibitors of AChE. Previous studies have demonstrated their highly selective and effective inhibition of AChE. Here, they were used as positive control drugs to assess the selectivity of ROCMCBs. Moreover, nitrofurazone, oxytetracycline, and indomethacin were randomly selected as negative controls. These compounds represent distinct mechanisms of action. Nitrofurazone is used as an antibacterial agent[42], oxytetracycline serves as a broad-spectrum antibiotic[43], and indomethacin targets cyclooxygenase to alleviate inflammation[44]. Using them as negative controls assisted in confirming the specificity of AChE activity, ensuring that the observed electrochemical responses were not generic reactions common to other widely used drugs. As shown in Fig. 5F, only positive drugs (huperzine A and galanthamine) exhibited significant inhibition rates on ROCMCBs (79.3% and 72.3%), and another three drugs showed low inhibition rates on ROCMCBs (2.0%, 5.8%, and 2.9%). Moreover, the inhibition rates of huperzine A on ROCMCBs and CMCBs were 79.3% and 64.6%, respectively, which showed the superiority of the right-side-out-oriented coating method of ROCMCBs. These results confirmed the selectivity of ROCMCBs towards AChE inhibitors.

Subsequently, the same procedure was used to prepare five batches of ROCMCBs, which exhibited highly consistent responses in repeatability tests. As illustrated in Fig. 5G, the relative standard deviation (RSD) of current at 650 mV of ROCMCBs was 3.39% (the current response values for ATCl across the five sets of ROCMCBs ranged from 4.149 to 3.978), while that of CMCBs was 7.07%. This high level of repeatability ensured the accuracy and reliability of ROCMCBs, providing a solid foundation for

drug evaluation in real applications. Then, in order to determine the durability of ROCMCBs during storage, the inhibition responses of 4.1 μmol/L huperzine A on ROCMCBs and CMCBs were measured daily. As shown in Fig. 5H, after 7 days of storage, the average inhibition rate of ROCMCBs remained at approximately 72% of the initial value. Surprisingly, the average inhibition rate of CMCBs dropped to around 27% of the initial value, which indicated that ROCMCBs possessed significantly better storage stability compared to CMCBs, thereby ensuring consistently reliable results over extended storage periods.

3.8. Molecular docking study

TCMs are renowned for their unique characteristics of multi-component, multi-pathway, and multi-target effects. Therefore, screening for active compounds from TCMs that target specific sites is of paramount importance[45]. Molecular docking was utilized to discover potentially active compounds from TCMs. Here, eight ingredients of TCMs that showed therapeutic effects on AD according to previous studies were selected, which were baicalin[46], geniposide[47], gastrodin[48], berberine[49], rhynchophylline[50], senkyunolide A[51], tanshinone IIA[52], and echinacoside[53]. Eight compounds were docked to AChE using the Surflex-Dock mode of SYBYL-X 2.0 to predict the inhibition behavior of the potentially active compounds against AD. All compounds and the positive drug huperzine A docked with the AChE active site (PDB ID: 1VOT). The total scores of the molecular docking were shown in Supporting Information Table S3. Fig. 6A illustrated that the amino acid residues of AChE that interact with huperzine A include TYR 121 and GLU 199. Fig. 6B–D showed the simulated binding of baicalin, geniposide, and gastrodin. TYR 121 and GLU 199 from baicalin-AChE binding (Fig. 6B), GLU 199 from geniposide-AChE binding (Fig. 6C), and GLU 199 from gastrodin-AChE binding (Fig. 6D) were the same as huperzine A-AChE binding. Meanwhile, Supporting Information Fig. S6–S8 showed the simulated binding of berberine (Fig. S6), senkyunolide A (Fig. S7), and rhynchophylline (Fig. S8). The molecular docking total scores of the six compounds were all above 4 points,

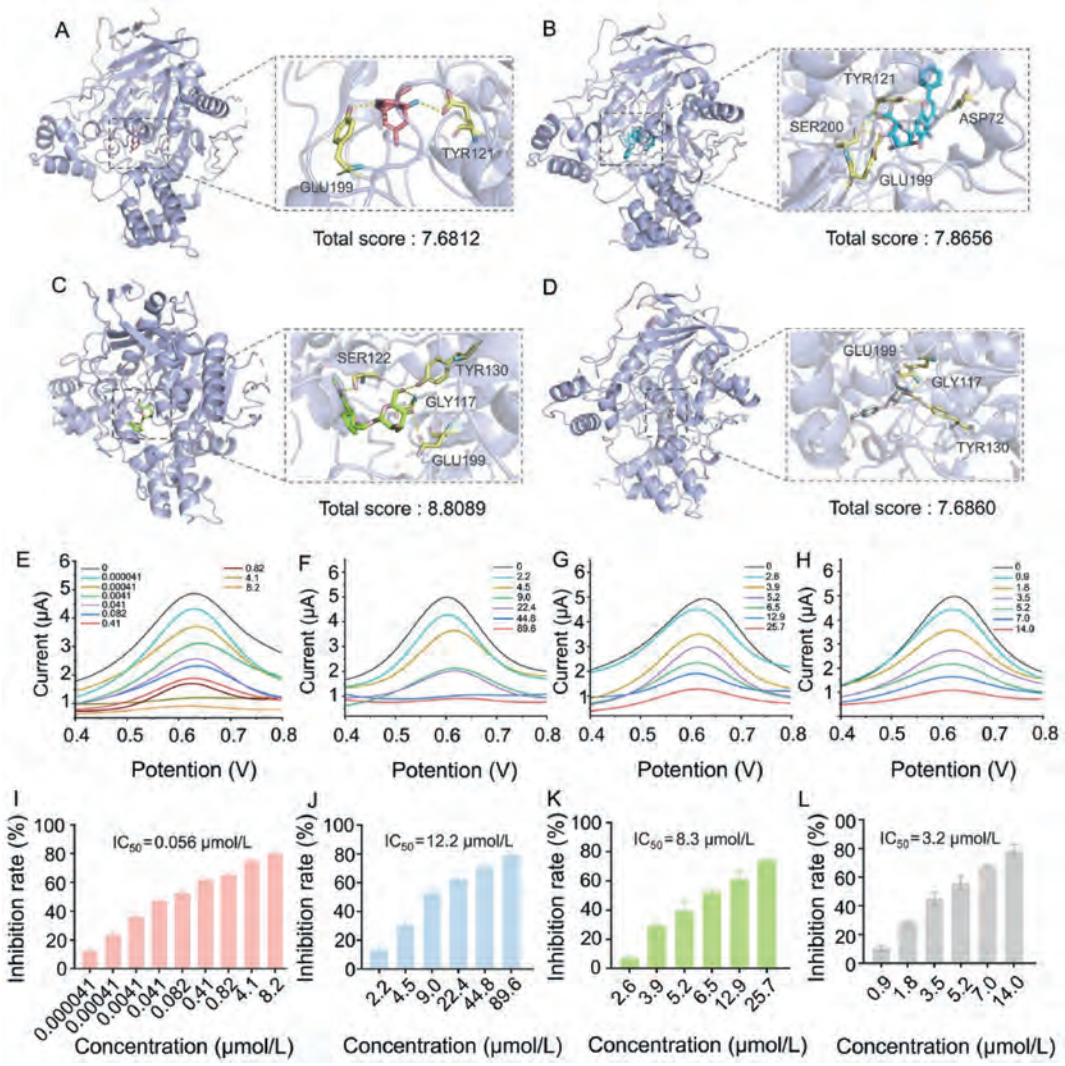

Figure 6 Molecular docking study and inhibitors evaluation on ROCMCBs. Molecular docking results of (A) huperzine A, (B) baicalin, (C) geniposide, and (D) gastrodin (PDB ID: 1VOT). DPV curves of (E) huperzine A, (F) baicalin, (G) geniposide, and (H) gastrodin in different concentrations (μmol/L). Concentrations of (I) huperzine A, (J) baicalin, (K) geniposide, and (L) gastrodin *versus* inhibition rates (μmol/L). Data are presented as mean ± SD ($n = 3$).

proving that they were all potential anti-AD active compounds. Furthermore, Supporting Information Fig. S9 illustrated the simulated binding of tanshinone IIA, revealing that its binding mode was dissimilar to that of the binding pocket of huperzine A. The molecular docking total score of tanshinone IIA was less than 4 points, and the molecular docking total score of echinacoside was −13.6492, indicating that these two compounds interacted with AChE in a relatively weak manner. In light of the aforementioned docking results, baicalin, geniposide, gastrodin, berberine, rhynchophylline, and senkyunolide A were initially identified as potential selective AChE inhibitors.

3.9. Inhibitors' evaluation of ROCMCBs

ROCMCBs were utilized to evaluate potentially active compounds from TCMs according to the results of molecular docking. The inhibitory effects of various concentrations of different ingredients on AChE currents were observed using the DPV test, and their IC_{50} values were calculated. The results were presented in Fig. 6E−L and Supporting Information Figs. S10−S17. It was obvious that the inhibitory effects of huperzine A (Fig. 6E and I), baicalin (Fig. 6F and J), geniposide (Fig. 6G and K), gastrodin (Fig. 6H and L), berberine (Figs. S10 and S13), senkyunolide A (Figs. S11 and S14), and rhynchophylline (Figs. S12 and S15) on AChE increased as the drug concentration increased, and their IC_{50} on AChE were 0.056, 12.2, 8.3, 3.2, 4.7, 86.6, and 66.3 μmol/L, respectively. However, tanshinone IIA (Fig. S16) and echinacoside(Fig. S17) did not show significant AChE inhibition effects under the same conditions. Therefore, it could be inferred that baicalin, geniposide, gastrodin, berberine, senkyunolide A, and rhynchophylline were likely to play an anti-AD role by inhibiting the activity of AChE, while tanshinone IIA and echinacoside were not. The above results correspond to their molecular docking results, demonstrating the potential of ROCMCBs in the identification of inhibitors of AChE. This approach not only enabled the evaluation of compounds that may inhibit AChE activity but also provided valuable insights into the mechanisms through which these compounds might operate as therapeutic agents for AD.

4. Conclusions

In this study, we introduced a novel method for right-side-out-oriented RBCM coating of electrochemical biosensors based on immunoaffinity, enabling the efficient evaluation of AChE inhibitors from TCMs and assessing their potential effectiveness as anti-AD drugs. The specific immunoaffinity was utilized to ensure the right-side-out orientation of RBCM, providing an effective method for evaluating AChE inhibitors. The experimental results demonstrated that this strategy ensured the directionality and stability of the RBCM coating, thereby preserving the activity of the peripheral membrane-anchoring protein. Consequently, six potentially anti-AD active compounds, including baicalin, geniposide, gastrodin, berberine, rhynchophylline, and senkyunolide A, were successfully evaluated by ROCMCBs based on AChE activity. The evaluation results correlated well with molecular docking simulations, highlighting the efficacy of the prepared biosensors in accurately monitoring AChE activity inhibited by potentially active compounds in TCMs. In conclusion, this strategy represents a novel technique for precise bionic design in the electrochemical drug evaluation from TCMs. This innovative approach not only facilitates the exploration of cell membrane coating technologies but also holds significant potential for accelerating the evaluation process of AChE inhibitors and the treatment of AD.

Acknowledgments

We gratefully acknowledge the National Natural Science Foundation of China (Nos. 82104125 and 82373832), China Postdoctoral Science Foundation (No. 2021M702632), and Key Research and Development Projects of Shaanxi Province (Nos. 2023-YBSF-145, 2024SF-YBXM-469, and 2024JC-YBMS-651).

Author contributions

Ying Zhao carried out the experiments, performed data analysis, and wrote the manuscript. Xia Liu, Shuning Yang, Jiabo Wang, and Dan Wu participated in part in the experiments. Yusi Bu and Xiaoyu Xie designed the study and revised the manuscript. All of the authors have read and approved the final manuscript.

Conflicts of interest

The authors have no conflicts of interest to declare.

Appendix A. Supporting information

Supporting information to this article can be found online at https://doi.org/10.1016/j.apsb.2025.09.032.

References

1. Idoia G, Ilia VB, Laura S, Gustavo P, José Luis P. Therapeutic opportunities and delivery strategies for brain revascularization in stroke, neurodegeneration, and aging. *Pharmacol Rev* 2022;**74**:439.
2. Goedert M. Alzheimer's and Parkinson's diseases: the prion concept in relation to assembled Aβ, tau, and α-synuclein. *Science* 2015;**349**:1255555.
3. Mei F, Zhao C, Li SJ, Xue ZP, Zhao YY, Xu YH, et al. *Ngfr*$^{+}$ cholinergic projection from SI/nBM to mPFC selectively regulates temporal order recognition memory. *Nat Commun* 2024;**15**:7342.
4. Judd JM, Winslow W, Jasbi P, Klein-Seetharaman J, Velazquez R. Low circulating choline levels correlate with Alzheimer's disease pathology severity and cognitive impairment. *Alzheimer's Dement* 2023;**19**:e077122.
5. Luque FJ, Muñoz-Torrero D. Acetylcholinesterase: a versatile template to coin potent modulators of multiple therapeutic targets. *Acc Chem Res* 2024;**57**:450−67.
6. Li X, Li W, Tian PF, Tan TW. Delineating biosynthesis of Huperzine A, A plant-derived medicine for the treatment of Alzheimer's disease. *Biotechnol Adv* 2022;**60**:108026.
7. Nikolopoulos D, Manolakou T, Filia A, Nakos-Bimpos M, Polissidis A, Boumpas D. Hippocampal immune cell trafficking and a myeloid predominant inflammatory response with enhanced antigen presentation and decreased levels of neurotransmitters underly the neuropsychiatric phenotype of the NZW/NZB murine lupus model. *Ann Rheum Dis* 2021;**80**:21−2.
8. Geng HM, Tsang M, Subbaraj L, Cleveland J, Chen LJ, Lu M, et al. Tumor metabolism and neurocognition in CNS lymphoma. *Neuro Oncol* 2021;**23**:1668−79.
9. Bade A, Yadav P, Zhang L, Naidu Bypaneni R, Xu M, Glass TE. Imaging neurotransmitters with small-molecule fluorescent probes. *Angew Chem Int Ed* 2024;**63**:e202406401.
10. Liu EYL, Xia YJ, Kong XP, Guo MSS, Yu AXD, Zheng BZY, et al. Interacting with α7 nachr is a new mechanism for AChE to enhance

the inflammatory response in macrophages. *Acta Pharm Sin B* 2020; **10**:1926−42.
11. Loganathan C, Sakayanathan P, Thayumanavan P. Isolation of bioactive components from *Corallocarpus epigaeus* tuber and inhibitory potential against various molecular forms of acetylcholinesterase. *Alzheimer's Dement* 2020;**16**:e043402.
12. Fang RH, Gao W, Zhang L. Targeting drugs to tumours using cell membrane-coated nanoparticles. *Nat Rev Clin Oncol* 2023;**20**: 33−48.
13. Chai XY, Gu YQ, Lv L, Chen C, Feng F, Cao Y, et al. Screening of immune cell activators from Astragali Radix using a comprehensive two-dimensional NK-92MI cell membrane chromatography/C_{18} column/time-of-flight mass spectrometry system. *J Pharm Anal* 2022; **12**:725−32.
14. Xiong JQ, Wu M, Chen JL, Liu YF, Chen YR, Fan GL, et al. Cancer-erythrocyte hybrid membrane-camouflaged magnetic nanoparticles with enhanced photothermal-immunotherapy for ovarian cancer. *ACS Nano* 2021;**15**:19756−70.
15. Nguyen PHD, Jayasinghe MK, Le AH, Peng B, Le MTN. Advances in drug delivery systems based on red blood cells and their membrane-derived nanoparticles. *ACS Nano* 2023;**17**:5187−210.
16. Bai Y, Chen JQ, Zhang ST, Xu GY, Mao ZW, Ding Y, et al. Inflammation-responsive cell membrane-camouflaged nanoparticles against liver fibrosis *via* regulating endoplasmic reticulum stress and oxidative stress. *Adv Mater* 2024;**36**:2310443.
17. Yaman S, Ramachandramoorthy H, Iyer P, Chintapula U, Nguyen T, Sabnani M, et al. Targeted chemotherapy *via* HER2-based chimeric antigen receptor (CAR) engineered T-cell membrane coated polymeric nanoparticles. *Bioact Mater* 2024;**34**:422−35.
18. Wang B, Yang PB, Ding YX, Qi HL, Gao Q, Zhang CX. Improvement of the biocompatibility and potential stability of chronically implanted electrodes incorporating coating cell membranes. *ACS Appl Mater Interfaces* 2019;**11**:8807−17.
19. Dong LL, Ren SX, Zhang XQ, Yang YT, Wu QL, Lei TZ. *In-situ* synthesis of Pt nanoparticles/reduced graphene oxide/cellulose nanohybrid for nonenzymatic glucose sensing. *Carbohydr Polym* 2023;**303**: 120463.
20. Zhang XL, Zhen XY, Yang YX, Feng Q, Yuan WQ, Xie XY. Precise assembly of inside-out cell membrane camouflaged nanoparticles *via* bioorthogonal reactions for improving drug leads capturing. *Acta Pharm Sin B* 2023;**13**:852−62.
21. Zhang YX, Fan F, Chai YF, Chen XF. Biosensing materials for monoclonal antibody detection: an overview. *Responsive Mater* 2024; **2**:e20240006.
22. Gu YQ, Fan F, Liu Y, Chai YF, Yuan YF, Chen XF. Cell-free protein synthesis system for bioanalysis: advances in methods and applications. *TrAC-Trend Anal Chem* 2023;**161**:117015.
23. Vargas E, Zhang FY, Ben Hassine A, Ruiz-Valdepeñas Montiel V, Mundaca-Uribe R, Nandhakumar P, et al. Using cell membranes as recognition layers to construct ultrasensitive and selective bioelectronic affinity sensors. *J Am Chem Soc* 2022;**144**: 17700−8.
24. Lu ZX, Bai S, Jiang YH, Wu SY, Xu DZ, Zhang JZ, et al. Amplifying dendritic cell activation by bioinspired nanometal organic frameworks for synergistic sonoimmunotherapy. *Small* 2022;**18**: 2203952.
25. Sato YT, Umezaki K, Sawada S, Mukai S, Sasaki Y, Harada N, et al. Engineering hybrid exosomes by membrane fusion with liposomes. *Sci Rep* 2016;**6**:21933.
26. Hu CMJ, Zhang L, Aryal S, Cheung C, Fang RH, Zhang L. Erythrocyte membrane-camouflaged polymeric nanoparticles as a biomimetic delivery platform. *Proc Natl Acad Sci U S A* 2011;**108**: 10980−5.
27. Gu YQ, Chen X, Wang Y, Liu Y, Zheng LY, Li XQ, et al. Development of 3-mercaptopropyltrimethoxysilane (MPTS)-modified bone marrow mononuclear cell membrane chromatography for screening anti-osteoporosis components from Scutellariae Radix. *Acta Pharm Sin B* 2020;**10**:1856−65.
28. Bu YS, Wu D, Zhao Y, Wang GX, Dang XT, Xie XY, et al. Genetically engineered cell membrane-coated nanoparticles with high-density customized membrane receptor for high-performance drug lead discovery. *ACS Appl Mater Interfaces* 2023; **15**:52150−61.
29. Gu YQ, Wang R, Chen PP, Li SN, Chai XY, Chen C, et al. *In situ* synthesis and unidirectional insertion of membrane proteins in liposome-immobilized silica stationary phase for rapid preparation of microaffinity chromatography. *Acta Pharm Sin B* 2022;**12**:3682−93.
30. Bu YS, Zhang XL, Zhu AH, Li LH, Xie XY, Wang SC. Inside-out-oriented cell membrane biomimetic magnetic nanoparticles for high-performance drug lead discovery. *Anal Chem* 2021;**93**: 7898−907.
31. Fenalti G, Villanueva N, Griffith M, Pagarigan B, Lakkaraju SK, Huang RYC, et al. Structure of the human marker of self 5-transmembrane receptor CD47. *Nat Commun* 2021;**12**:5218.
32. Tang L, Yin Y, Cao YQ, Fu C, Liu HN, Feng JW, et al. Extracellular vesicles-derived hybrid nanoplatforms for amplified CD47 blockade-based cancer immunotherapy. *Adv Mater* 2023;**35**:2303835.
33. Fang RH, Kroll AV, Gao W, Zhang L. Cell membrane coating nanotechnology. *Adv Mater* 2018;**30**:1706759.
34. Inkpen MS, Liu ZF, Li H, Campos LM, Neaton JB, Venkataraman L. Non-chemisorbed gold−sulfur binding prevails in self-assembled monolayers. *Nat Chem* 2019;**11**:351−8.
35. Lee JH, Choi HK, Yang L, Chueng STD, Choi JW, Lee KB. Nondestructive real-time monitoring of enhanced stem cell differentiation using a graphene-Au hybrid nanoelectrode array. *Adv Mater* 2018;**30**: 1802762.
36. Li HF, Liu ZX, Liang GJ, Huang Y, Huang Y, Zhu MS, et al. Waterproof and tailorable elastic rechargeable yarn zinc ion batteries by a cross-linked polyacrylamide electrolyte. *ACS Nano* 2018;**12**: 3140−8.
37. Kim I, Kwon D, Lee D, Lee G, Yoon DS. Permselective glucose sensing with GLUT1-rich cancer cell membranes. *Biosens Bioelectron* 2019;**135**:82−7.
38. Liu XM, Xiao TF, Wu F, Shen MY, Zhang MN, Yu HH, et al. Ultrathin cell-membrane-mimic phosphorylcholine polymer film coating enables large improvements for *in vivo* electrochemical detection. *Angew Chem Int Ed* 2017;**56**:11802−6.
39. Lian ML, Shi YQ, Chen LX, Qin YJ, Zhang W, Zhao JB, et al. Cell membrane and V_2C MXene-based electrochemical immunosensor with enhanced antifouling capability for detection of CD44. *ACS Sens* 2022;**7**:2701−9.
40. Jiang YJ, Zhang XN, Pei LJ, Yue S, Ma L, Zhou LY, et al. Silver nanoparticles modified two-dimensional transition metal carbides as nanocarriers to fabricate acetycholinesterase-based electrochemical biosensor. *Chem Eng J* 2018;**339**:547−56.
41. Atri A, Frölich L, Ballard C, Tariot PN, Molinuevo JL, Boneva N, et al. Effect of idalopirdine as adjunct to cholinesterase inhibitors on change in cognition in patients with Alzheimer disease: three randomized clinical trials. *JAMA* 2018;**319**:130−42.
42. Yin XC, Deng ZA, Dou LN, Guo J, Yang CY, Dai Z, et al. Cascaded antibody directionality relying on a zinc-based nanocomposite for performance enhancement of multiplex lateral flow immunoassay. *Chem Eng J* 2024;**481**:148493.
43. Zhang P, Xu L, Su JF, Zeng YX, Liu Y, Li X. Simultaneous removal of nitrate, oxytetracycline and copper by ferrous-manganese co-driven immobilized bioreactor. *J Hazard Mater* 2024;**466**:133621.
44. Elmunzer BJ, Foster LD, Serrano J, Coté GA, Edmundowicz SA, Wani S, et al. Indomethacin with or without prophylactic pancreatic stent placement to prevent pancreatitis after ercp: a randomised non-inferiority trial. *Lancet* 2024;**403**:450−8.
45. Wang HR, Gu YQ, Khalid R, Chen XF, Han T. Herbal medicines for insomnia through regulating 5-hydroxytryptamine receptors: a systematic review. *Chin J Nat Med* 2023;**21**:483−98.
46. Durmaz L, Karagecili H, Gulcin I. Evaluation of carbonic anhydrase, acetylcholinesterase, butyrylcholinesterase, and α-glycosidase inhibition effects and antioxidant activity of baicalin hydrate. *Life* 2023;**13**:2136.

47. Wang L, Yan SJ, Zhang WS. Effects of an early-and late-stage treatment with geniposide on cognitive dysfunction in a transgenic mouse model relevant to Alzheimer's disease. *Mol Neurodegener* 2012;**7**:S4.
48. Su ZH, Yang YG, Xu HB, Tang ZS, Sun MN, Zhu YY, et al. Study on the chemical composition and *in vitro* enzyme inhibition of different processed products of *Gastrodia elata*. *J Food Compos Anal* 2024;**130**: 106148.
49. Leimann FV, de Souza LB, de Oliveira BPM, Rossi BF, da Silva PS, Shiraishi CSH, et al. Evaluation of berberine nanoparticles as a strategy to modulate acetylcholinesterase activity. *Food Res Int* 2023;**173**:113295.
50. Chear NJ, Ching-Ga TA, Khaw KY, León F, Tan WN, Yusof SR, et al. Natural corynanthe-type cholinesterase inhibitors from Malaysian Uncaria attenuata Korth.: isolation, characterization, *in vitro* and *in silico* studies. *Metabolites* 2023;**13**:390.
51. Wu WH, Liang XT, Xie GQ, Chen LD, Liu WX, Luo GL, et al. Synthesis and evaluation of novel ligustrazine derivatives as multi-targeted inhibitors for the treatment of Alzheimer's disease. *Molecules* 2018;**23**:2540.
52. Liu C, Wu YX, Zha S, Liu MP, Wang Y, Yang GD, et al. Treatment effects of tanshinone IIA against intracerebroventricular streptozotocin induced memory deficits in mice. *Brain Res* 2016;**1631**:137−46.
53. Ding L, Ye H, Gu LD, Du AQ, Yuan XL. Echinacoside alleviates cognitive impairment in cerebral ischemia rats through α 7nAChR-induced autophagy. *Chin J Integr Med* 2022;**28**:809−16.